Parameterization of Mixed Layer Eddies. I: Theory and Diagnosis

BAYLOR FOX-KEMPER

Department of Earth, Atmospheric and Planetary Sciences, Massachusetts Institute of Technology, Cambridge, Massachusetts, 01239

RAFFAELE FERRARI

Department of Earth, Atmospheric and Planetary Sciences, Massachusetts Institute of Technology, Cambridge, Massachusetts, 01239

ROBERT HALLBERG

NOAA Geophysical Fluid Dynamics Laboratory, Princeton, New Jersey

(8 October 2007)

ABSTRACT

Ageostrophic baroclinic instabilities develop within the surface mixed layer of the ocean at horizontal fronts and efficiently restratify the upper ocean. In this paper a parameterization for the restratification driven by finite-amplitude baroclinic instabilities of the mixed layer is proposed in terms of an overturning streamfunction that tilts isopycnals from the vertical to the horizontal. The streamfunction is proportional to the product of the horizontal density gradient, the mixed layer depth squared, and the inertial period. Hence restratification proceeds faster at strong fronts in deep mixed layers with a weak latitude dependence. In this paper the parameterization is theoretically motivated, confirmed to perform well for a wide range of mixed layer depths, rotation rates, and vertical and horizontal stratifications. It is shown to be superior to alternative extant parameterizations of baroclinic instability for the problem of mixed layer restratification. Two companion papers discuss the numerical implementation and the climate impacts of this parameterization.

1. Introduction

A typical oceanic stratification and shear allows two types of baroclinic instability (Boccaletti et al., 2007, hereafter BFF): deep mesoscale instabilities spanning the entire depth and shallow submesoscale instabilities trapped in the weakly-stratified surface mixed layer (ML). The troposphere and its surface boundary layer provide two analogous types of instability (Blumen, 1979; Nakamura, 1988). The shallow ML instabilities are ageostrophic baroclinic instabilities (Stone, 1966, 1970, 1972a; Molemaker et al., 2005) and differ from the deep mesoscale instabilities in their fast growth rates of O(1/day) and small scales of O(1 km). BFF suggest that ML instabilities play an important role in restratifying the upper ocean after strong mixing events.

Presently ocean models use a variety of boundary layer parameterizations to represent the pro-

cesses that mix away stratification in response to surface forcing (e.g., Kraus and Turner, 1967; Price, 1981; Price et al., 1986; Large et al., 1994; Thomas, 2005), while ML restratification occurs only by surface heating. Dynamical restratification by slumping of horizontal density gradients within the ML is typically ignored. As a consequence, ocean models have a bias towards weak near-surface stratification (*e.g.,* Oschlies, 2002; Hallberg, 2003; Chanut et al., 2005). Large-scale ocean models are beginning to resolve deep mesoscale eddies with O(10km) grids, but resolving restratification by submesoscale instabilities requires O(100m) grids. Submesoscale instabilities are subgridscale even in "eddy-resolving" models.

In this paper scalings are developed for restratification by finite-amplitude ML instabilities, herein referred to as mixed layer eddies (MLEs). These scalings are tested in idealized simulations and formulated into a parameterization. Two companion papers provide more insight into the workings of the parameterization. Fox-Kemper and Ferrari (2007,

---

hereafter FF) compare the parameterization with submesoscale-resolving simulations and estimate the importance of MLE restratification from data. The numerical implementation of the parameterization and its effects in realistic global simulations are the subject of a third paper (Fox-Kemper et al., 2007).

Tandon and Garrett (1994) first proposed that dynamical restratification occurs at lateral density fronts in the ML after strong mixing events. However they considered only restratification by Rossby adjustment of lateral fronts (Rossby, 1937, 1938; Ou, 1984; Tandon and Garrett, 1995). Young (1994) and Hallberg (2003) derive parameterizations for the restratification by Rossby adjustment. However, BFF show that most dynamical restratification occurs after the initial Rossby adjustment, when ML instabilities reach finite amplitude and start releasing the potential energy (PE) stored in the front.

The parameterization developed here represents the restratification by ML instabilities. Following Gent and McWilliams (1990) (henceforth GM), the restratification is cast in terms of an eddy-induced streamfunction that adiabatically overturns isopycnals from the vertical to the horizontal. Scalings are derived directly for the overturning streamfunction, in contrast to the traditional approach of using mixing length arguments to relate fluxes to mean gradients via an effective diffusivity. The proposed scaling depends only on finite-amplitude properties of MLEs that are confirmed by simulations.

There are many notable studies of baroclinic instabilities in the ML. References for the linear analysis are given in BFF. This work is closer in spirit to previous studies at finite amplitude (Samelson and Chapman, 1995; Spall, 1997; Jones and Marshall, 1993, 1997; Haine and Marshall, 1998). However, the focus here is a parameterization of ML restratification which does not appear elsewhere. It will be shown that MLEs restratify importantly through an upward buoyancy flux; capturing MLE horizontal fluxes is less important. The strength of the vertical fluxes is predicted by the parameterization as a function of the lateral frontal buoyancy gradient and the ML depth. The parameterization applies to restratification by the submesoscale eddies observed throughout the extratropics (Weller, 1991; Rudnick and Ferrari, 1999; Hosegood et al., 2006). The parameterization also recovers the scaling laws found by Jones and Marshall (1997) and Haine and Marshall (1998) for eddy transport and restratification during deep convection at high latitudes.

The paper is structured as follows. Section 2 gives a relevant phenomenology of MLEs through study of two idealized numerical simulations. Section 3 presents the theory behind the parameterization. Section 4 validates the parameterization by diagnosis of the simulations. Concluding remarks and a review of observational evidence of ML restratification are presented in section 5.

2. Phenomenology of MLEs

Two numerical simulations are used to gain a sense of the phenomenology of MLEs. The first contrasts and connects mesoscale eddies and submesoscale MLEs. The second focuses on MLE restratification at a single front.

a. Simulation with both Mesoscale and Submesoscale Eddies

The first simulation is configured to produce deep mesoscale eddies extending through the whole water column and shallow submesoscale eddies trapped in the surface ML. The MITgcm model (Marshall et al., 1997) is configured to simulate a reentrant channel where a baroclinically unstable jet is maintained by restoring temperature profiles along the side walls (Fig. 1). The upper 75 m are initially unstratified, and are subsequently mixed by a diurnal cycle of 200W/m^2 cooling compensated by penetrating heating during the day. Nightly cooling thoroughly mixes the ML to roughly 50m depth. The simulation is run at 8km resolution for 900 days, interpolated to 2km resolution, and continued for 100 days. At this resolution, the largest MLEs[1] are permitted but only marginally resolved in order to permit mesoscale features as well. Below, dedicated simulations of MLEs alone allow better resolution of submesoscale features. Details are in Appendix A.

A vigorous mesoscale eddy field develops throughout the full water column (Fig. 1b), while variability in the ML is dominated by small-scale meandering fronts (Fig. 1a). The tightly packed isotherms result from straining by the mesoscale eddies and frontogenetic processes compacting outcropping isotherms. The meanders that develop along the fronts are MLEs. The large mesoscale eddies result from baroclinic instability of the mean jet with growth rates of O(1 month) and length scales near O(80 km). The smaller MLEs result from ageostrophic baroclinic instabilities that develop along fronts within the ML. Their scales begin near the linear instability scale based on ML depth and stratification,

---

[1]MLEs vary in size according to the strength of the front upon which they grow, see (2).
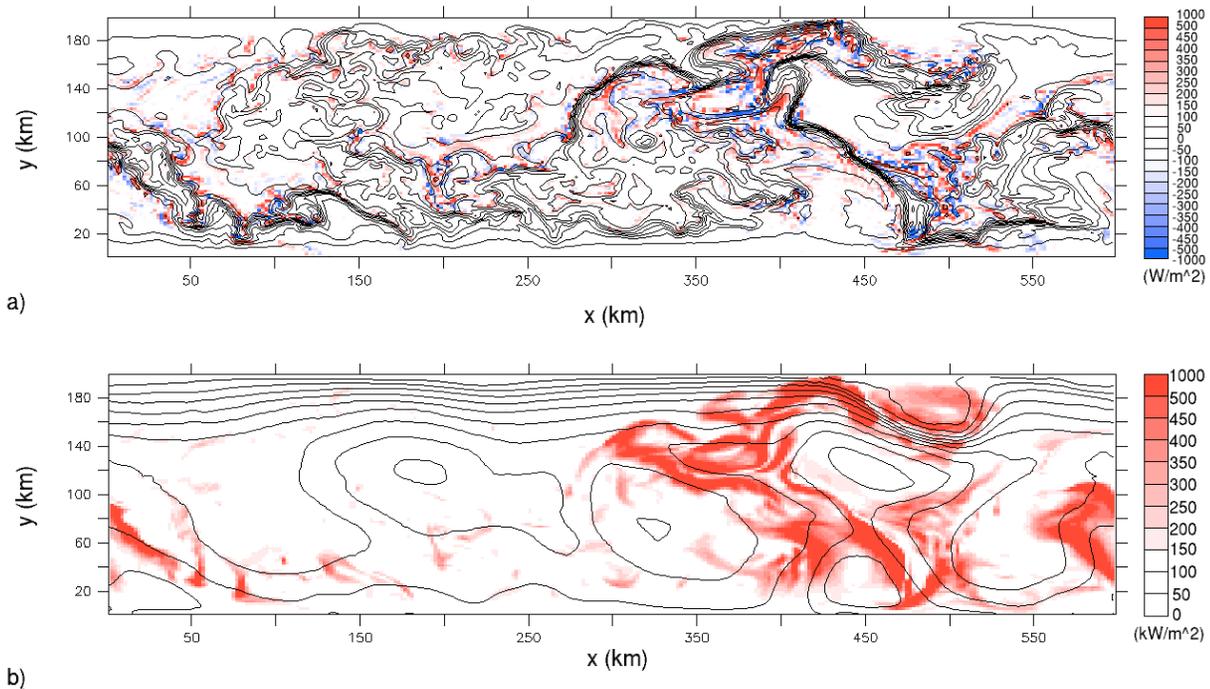
FIGURE 1: Contours of temperature at the a) surface and b) below the ML base in a simulation with both mesoscale eddies and MLEs (0.2°C contour intervals). Shading indicates $w'b'$ (upper panel) and $|\mathbf{u}'_H b'|$ (lower panel) at 20m depth, the depth at which eddy fluxes are largest.

O(1 to 5 km), and enlarge as a result of an inverse cascade as discussed in BFF. MLEs cluster along fronts, where frontal vertical shear endows the fastest growth (Stone, 1966). Elsewhere the growth rates are too slow to compete with the damping due to turbulent mixing.

BFF argue that the ML instability linear growth rates are only weakly affected by large scale straining, yet Spall (1997) shows that a large scale strain can substantially alter finite-amplitude baroclinic instability. This effect is notable in Fig. 1a near (450, 80) km, where a powerful surface temperature front is pinched between three mesoscale eddies (Fig. 1b). MLEs develop only after the front exits the strain field near (400, 140) km. The strain rates in this idealized simulation are larger than is typical in the real ocean, yet MLEs are present throughout the domain. Thus, while mesoscale straining can occasionally suppress MLEs, the effect is confined to the regions of largest convergence.

Basin-wide restratification can occur only by a net upward transport of buoyancy. That is, on the whole, the near-surface ML is made more buoyant and the deeper ML becomes denser. The vertical eddy buoyancy flux, $w'b'$, is shaded in Fig. 1a. (Primes denote departures from along-channel, $x-$direction averages. See Table 1). The figure shows fluxes near the depth where they are largest (20m). Two features emerge. First the largest vertical fluxes are small-scale features clustered near fronts. In fact, filtering w' and b' indicates that 70%(50%) of the basin average, $\overline{w'b'}^{xy}$, is generated by scales smaller than 12km (8km). (Overbars denote along-channel averages, and superscripts indicate additional averaging along other coordinates, See table 1). Second, $\overline{w'b'}^{xy}$ is positive rather than negative, implying a tendency to restratify the ML. The shading in Fig. 1b indicates regions where $|\mathbf{u}'_H b'|$ is largest. The horizontal fluxes are coherent on scales associated with mesoscale eddies, while the vertical fluxes are distinctly submesoscale. The mesoscale eddies and MLEs have comparable horizontal velocities, but mesoscale eddies stir over longer distances and dominate the horizontal fluxes. MLEs and fronts have larger Rossby number and thus larger vertical velocities, so they dominate the vertical fluxes. In sum, mesoscale eddies dominate the lateral fluxes while fronts and MLEs dominate vertical fluxes and restratification.

The role of MLEs in restratification is clarified by

comparing the simulation described above with an otherwise identical simulation run without a diurnal cycle from day 900 to day 1000. When the resolution is increased at day 900, near-surface restratification increases as a result of sharper fronts from mesoscale straining (Spall, 1997; Nurser and Zhang, 2000; Oschlies, 2002; Lapeyre et al., 2006). But, do MLEs and their associated fronts lead to even more restratification as suggested by BFF? With and without a continued diurnal cycle, the mesoscale eddies differ little and fronts of a similar strength develop at the surface–the averaged surface $|\nabla_H b|^2$ differs by less than 25%. But without a diurnal cycle the ML disappears through unchallenged restratification, and soon MLEs are stabilized. The average flux, $\overline{w'b'}^{xy}$, in the upper 40m is half (a third) that of the simulation with a continued diurnal cycle in ten (forty) days.

Some recent investigations without active remixing of the ML underestimate the restratification effect of MLEs (*e.g.,* Mahadevan, 2006; Mahadevan and Tandon, 2006), as MLEs do not occur after the ML has already restratified by other mechanisms. Other studies have found few or no MLEs because the ML in the regions considered were very shallow, so very high horizontal resolution would be required to resolve the instabilities (*e.g.,* Capet et al., 2006; Lapeyre et al., 2006). Of course, these simulations are not without near-surface restratification: frontogenesis, winds, and solar heating may all restratify. Ferrari and Thomas (2007) compare the relative contributions from these mechanisms quantitatively and conclude that MLEs play an important role in near surface restratification. MLE restratification is the subject of this paper.

b.   *Restratification by Spindown of a ML Front*

Frontal instabilities–MLEs–develop once the submesoscales are permitted (Fig. 1). However the computational expense of refining grid resolution to convergence for MLEs while retaining properly sized mesoscale eddies is onerous. Hence, the MLE restratification study continues by focusing on the spindown of a single ML front representing the aftermath of a mesoscale straining event as in Fig. 1 or the edge of a recent vertical mixing event (Price, 1981; Haine and Marshall, 1998). The front is initialized as a horizontal density gradient in a flat-bottom reentrant channel. Vertical stratification is uniform in the interior and weak in a surface ML. A typical model configuration is shown in Fig. 2a and detailed in Appendix B. The initial velocity may be

either resting (hereafter "unbalanced") or in thermal wind balance ("balanced"). Many other parameters vary across the simulations, and resolution is varied to ensure the baroclinic instability is resolved; tripling the resolution does not significantly change the results.

An unbalanced ML front first slumps gravitationally and oscillates inertially about the Rossby adjusted state (Tandon and Garrett, 1995). Soon afterward, ML instabilities are detectable. Within a few days they are evident as wavelike disturbances along the oscillating front (Fig. 2a) that enlarge in time (Figs. 2b-c). Five days are required to reach finite amplitude because the initial perturbations away from uniform flow in the along-channel direction are artificially small. In test simulations, and presumably also the ocean, larger initial perturbations develop into finite amplitude MLEs within one day. Balanced simulations do not undergo Rossby adjustment, but the development and nonlinear growth of ML instabilities is very similar. In all cases the initial PE is the primary energy source, and the MLEs grow by slumping the front to extract this energy (BFF).

MLE restratification increases the balanced Richardson number,

$$\text{Ri} \equiv N^2 \left| \frac{\partial \bar{\boldsymbol{u}}_g}{\partial z} \right|^{-2} = \frac{N^2 f^2}{M^4},$$

where N^2 and M^2 are volume-average values of b_z and b_y over the frontal region in the ML. The balanced Ri differs from the traditional Ri in that geostrophic shear replaces the full shear.

Fig. 3 shows the increase in Ri in four simulations. Two of the simulations have no initial velocity. The other two begin in thermal wind balance. In each pair, N^2 at $t = 0$ is set to either M^4/f^2 or 0.[2] The unbalanced simulations oscillate inertially near $\text{Ri} \approx 1$ for about 5 days, while the balanced simulation with $N^2 = 0$ develops symmetric instabilities in a few hours that then increase Ri to one. This early restratification is overwhelmed once MLEs are active (after day 5), and the MLE restratification rate $(\frac{\partial N^2}{\partial t})$ is the same once finite amplitude is reached. Only the time to reach finite amplitude differs: the larger Ri simulations reach finite amplitude later (as the linear growth rate (3) below predicts).[3] In sum-

---

[2] The initial Richardson number is $\text{Ri}_0 = 1$ or $\text{Ri}_0 = 0$, respectively. See Table 1 for notation.

[3] Symmetric instabilities are strengthened in a tripled resolution version of the balanced, $\text{Ri}_0 = 0$ case. At higher resolution, $\text{Ri} = 1$ is reached a day earlier, but the average restratification rate after $\text{Ri} > 2$ differs by less than 3%.
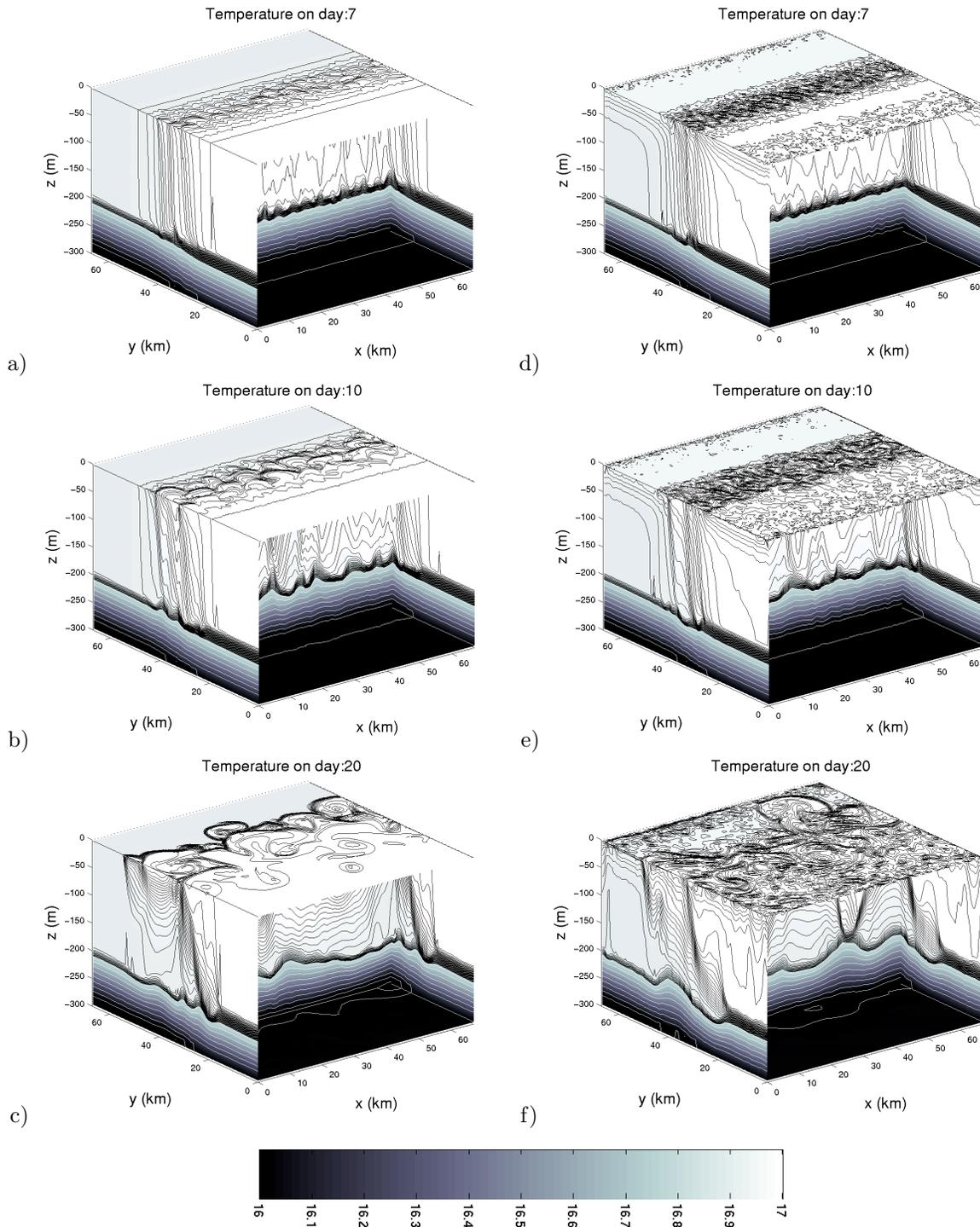
FIGURE 2: Temperature (^oC) during two typical simulations of a ML front spinning down: a-c) no diurnal cycle, d-f) with diurnal cycle and convective adjustment. (Black contour interval=0.01^{o}C, white contour interval=0.1^{o}C.)

mary, there are a variety of instabilities that rapidly bring the front to Ri $\approx$ 1, but the subsequent MLE restratification is insensitive to the details of these processes.

Ageostrophic baroclinic instabilities, which extract PE by slumping isopycnals, are the dominant
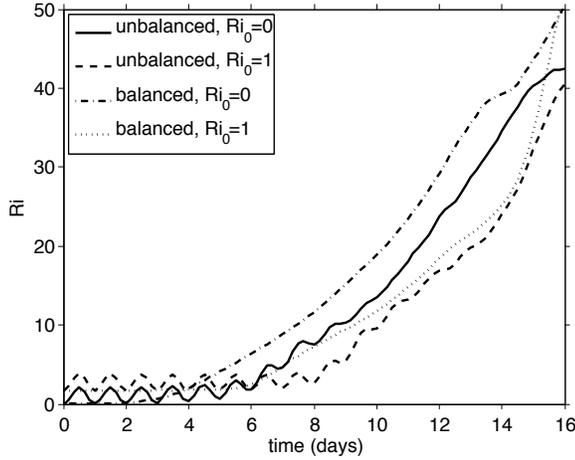
FIGURE 3: Balanced Richardson number for four simulations starting from a thermal wind "balanced" initial condition or resting initial velocity, *i.e.,*"unbalanced". All parameters are identical across simulations and at front center, but initial N^2 may be M_f^4/f^2 (labeled here as $\mathrm{Ri}_0 = 1$) or 0 ($\mathrm{Ri}_0 = 0$). N^2 is $\bar{b}_z$ averaged over the center of the front ($|y - y0| < L_f/4$), and M_f^4 is the largest value of $\bar{b}_y^2$ in the initial condition (Appendix B).

form of ML instabilities at Ri ≥ 1 (BFF, Haine and Marshall, 1998). Their main characteristics are captured by Stone (1970) in his analysis of the Eady (1949) problem. The linear growth rate is

$$\tau_s(k) = \frac{kU}{2\sqrt{3}}\left[1 - \frac{2k^2U^2}{15f^2}(1+\mathrm{Ri})\right], \qquad (1)$$

and the fastest growing mode has

$$L_s = \frac{2\pi}{k_s} = \frac{2\pi U}{|f|}\sqrt{\frac{1+\mathrm{Ri}}{5/2}}, \qquad (2)$$

$$\tau_s(k_s) = \sqrt{\frac{54}{5}}\frac{\sqrt{1+\mathrm{Ri}}}{|f|}. \qquad (3)$$

For the simulations shown in Fig. 2, $L_s = 3.9$ km and $\tau_s(k_s) = 16.8$hr for Ri $= 1$. MLEs appear near these scales in both the frontal spindown simulations (Fig. 2) and the mesoscale plus submesoscale simulation (Fig. 1a)–these values are much smaller and faster than those of mesoscale eddies.

The scales from linear theory are helpful in determining the numerical resolution necessary to permit MLEs, but they are not useful for parameterizing the frontal slumping effect of MLEs. Fig. 4 compares the power density spectrum of eddy kinetic energy (EKE) at various times from a nonlinear simulation and the linear theory prediction. Linear theory tracks the nonlinear spectrum only for the first
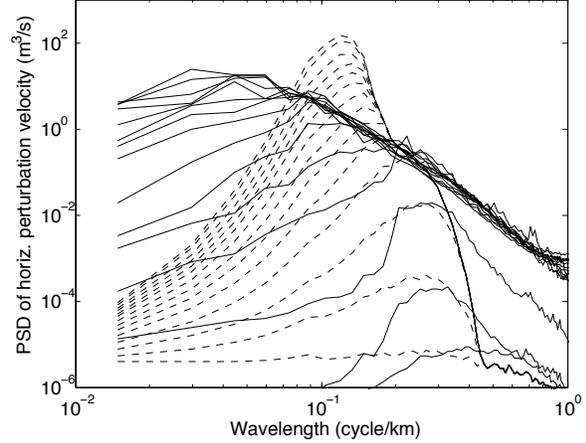
FIGURE 4: Perturbation power spectral density, $E(\kappa)$ for a simulation from Fig. 3 (solid). Spectra are plotted at two day intervals from day 1.5 to day 29.5. The linear prediction of the spectrum ($E_s(\kappa)$, dashed) is set equal to the nonlinear spectrum on day 1.5, and then evolved at each along-channel wavenumber as predicted by linear theory taking into account the changes in Ri and U. That is, $E_s(\kappa)$ is evolved using $\tau_s(k)$ from (1) based on the instantaneous Ri and U from the nonlinear simulation: $E_s(\kappa) = e^{2t/\tau_s(k)}\int E|_{t=1.5}(k,l)\mathrm{d}l$. The decrease in growth rate with cross-channel wavenumber, l, is ignored for simplicity and because low l modes soon dominate.

six days. During this period the spectral peak tracks the most unstable wavenumber predicted by (2) and shifts to larger scales because Ri grows as the stratification increases (Fig. 3). However the nonlinear spectrum departs the linear prediction as the instabilities reach finite amplitude. EKE is transferred to scales larger than the most unstable mode through a vigorous inverse cascade (Fig. 4).

The inverse cascade complicates the parameterization problem. Eddy mixing length arguments are routinely used to study baroclinic eddy fluxes (Haine and Marshall, 1998; Spall, 2000; Larichev and Held, 1995; Schneider and Walker, 2006). In these arguments the lateral transport of tracers is dominated by the largest energy-containing eddies (*e.g.,* Howells, 1960). The eddy saturation strength follows a simple scaling: the eddy velocity within the front saturates at the initial mean flow velocity as shown in Fig. 5 (Stone, 1972b). The mixing length, however, is not fixed in time in spindown problems such as this one, nor is it readily estimated from other horizontal scales: the most energetic eddies enlarge beyond the most unstable scale (*e.g.,* Cehelsky and Tung, 1991) and beyond the initial frontal width
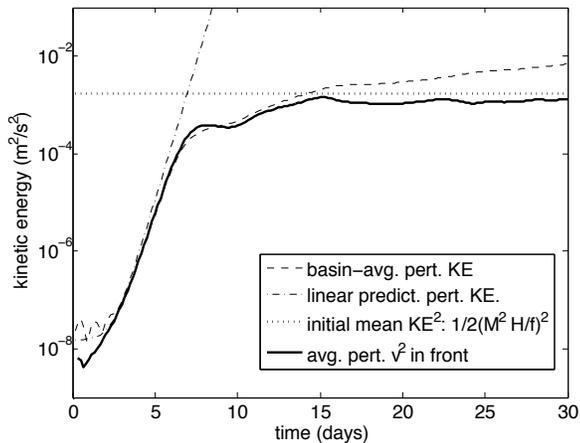
FIGURE 5: Kinetic energies and cross-channel perturbation velocity variance as a function of time from the same simulation as Fig. 3 (solid) and Fig. 4. The slight increase in the basin-average EKE after day 15 is simply a result of the enlarging eddy scale widening the area of eddy activity into previously motionless fluid (see Fig. 4). That is, the basin-average of perturbation KE continues to grow (dashed line) while the average over only the center of front saturates (solid line).

FIGURE 6: Typical vertical excursion scale, $\zeta \equiv \sqrt{\overline{b'^2}}/N^2$, scaled by ML depth, H, for initially balanced simulations where the initial ML depth was 200m (solid), balanced simulations where the ML depth was 50m (dashed), and unbalanced simulations where the initial ML depth was 200m (dotted). Other parameters vary as well: L_f/L_s varies by a factor of four and initial N is 0 or $4f$. The value of ζ/H shown is the maximum in z, horizontally-averaged over the front center.

(Fig. 2c).

Another popular approach for parameterizing baroclinic spindown relies on linear stability theory of the basic state (*e.g.,* Stone, 1972b; Killworth, 2005). The core assumptions are that eddies and mean state satisfy the same scaling and that finite-amplitude eddies resemble the fastest-growing linear instability. In the MLE problem, not only are longer lengthscales energized by the inverse cascade, but frontogenesis leads to smaller lengthscales as well. The mean state is well described by quasi-geostrophic (QG) scaling–perhaps modified to allow variable background stratification (*e.g.,* Nakamura and Held, 1989), but the MLE Richardson and Rossby numbers approach one as a result of frontogenesis at the boundaries. This spontaneous loss of balance is a distinguishing feature of fronts that outcrop at the ocean surface (Molemaker et al., 2005).

Nakamura and Held (1989) and Nakamura (1994) argue that the nonlinear, frontogenetic development of MLEs can be captured by stability analysis in geostrophic coordinates (Hoskins, 1976). This approach correctly predicts frontal development of Richardson and Rossby numbers of O(1). However, this approach also predicts that the ageostrophic shear generated through frontogenesis grows as large as the geostrophic shear and arrests further restratifi-

cation, as verified in 2d simulations by Nakamura (1994). In three dimensions restratification continues despite the appearance of fronts (Fig. 2); the MLEs twist and fold the front and prevent the frontogenetic two-dimensional saturation (as in Spall, 1997).

Traditional approaches therefore provide little guidance in developing a parameterization of frontal slumping and spindown by MLEs. There are however aspects of the nonlinear frontal spindown that can be used to develop a parameterization. First, the initially vertical isopycnals slump from the vertical to the horizontal without spreading much, *i.e.,* M^2 decreases only 10 to 20% while N^2 increases by orders of magnitude. Second, the inverse cascade proceeds to ever increasing scales in the horizontal, but it is arrested by the ML depth in the vertical. The typical vertical excursion scale is a fixed proportion of the ML depth across different simulations (Fig. 6). Third, the MLEs release PE by fluxing buoyancy along a surface at a shallower slope than the mean isopycnal surface (*i.e.,*the flux direction is more horizontal than the isopycnals), a characteristic of linear and nonlinear baroclinic instability (Fig. 7). The ratio of the slopes is fixed near two, the value yielding the maximum extraction of PE (Eady, 1949; Haine and Marshall, 1998). Fourth, the rms
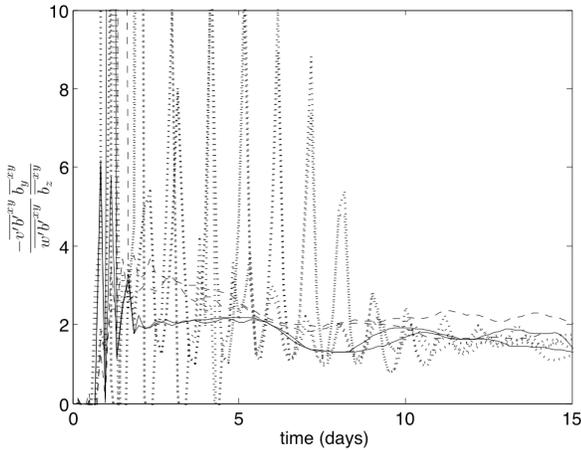
FIGURE 7: Ratio of the horizontal to vertical eddy fluxes scaled by isopycnal slope for the same simulations as in Fig. 6. The z-level shown is the ML midpoint, and all quantities are averaged over the center of the front.

FIGURE 8: Schematic of the ML restratification. Thin contours denote along-channel mean isopycnals. Straight arrows denote direction of the eddy buoyancy fluxes, and circular contours/arrows indicate eddy-induced streamfunction contours and direction. The decorrelation lengths of the eddies Δy and Δz are indicated. The reader is reminded that after Rossby adjustment the isopycnals are already flattened to slopes of O(10m per km) despite their near vertical appearance in this figure.

eddy velocities in the middle of the front saturate at a value that scales with the initial mean geostrophic shear (Fig. 5). These four elements constitute the basic ingredients of the parameterization.

3. Theory for the Parameterization

A parameterization of ML restratification is to be derived based on the phenomenology of MLEs. A schematic of the slumping process of a ML front is shown in Fig. 8. The vertical eddy buoyancy fluxes are everywhere positive, and the horizontal cross-channel eddy fluxes are everywhere down the mean horizontal gradient. The fluxes are along a shallower slope than the mean isopycnal slope to slump the front and reduce the mean PE.

The ML restratification problem shares many aspects with the mesoscale restratification considered by Gent and McWilliams (1990, hereafter GM) and Gent et al. (1995). First, restratification proceeds through baroclinic instabilities and releases mean PE. Second, isopycnal slumping is largely adiabatic and can be represented through advection by an eddy-driven overturning streamfunction. Third, momentum fluxes are weak compared to Coriolis forces, hence only buoyancy fluxes need to be parameterized. Despite these similarities, the GM parameterization is not optimal for MLE restratification for two reasons. The MLE vertical structure is dictated by the ML depth (Fig. 6); there is no such constraint in the ocean interior or GM. Second, the ML is frequently remixed, so M^2 is nearly depth-

independent. The Rossby adjustment or symmetric instabilities that follow remixing provide a nearly depth-independent N^2 from the depth-independent M^2. Hence, MLIs develop with nearly uniform background M^2 and N^2, which simplifies the parameterization.

It is an open question whether parameterization of mesoscale restratification should be cast in terms of PV[4] or PE budgets. During MLE restratification the horizontally-averaged PV outside of frictional layers is nearly uniform in the vertical. Thus,

$$\text{PE} \equiv \overline{-zb}^{xyz} \propto H^2 \overline{b_z}^{xyz} \approx H^2 \overline{\text{PV}}^{xyz}/f,$$

and the two approaches are equivalent. Lapeyre et al. (2006) note that frontogenesis can intensify PV near the surface without affecting PE. While this effect appears significant for mesoscale eddies, it is secondary for MLEs. We can therefore develop the parameterization using the along-channel mean buoyancy budget and the volume average PE budget (over a large volume containing the frontal slumping so that boundary terms vanish),

$$\frac{\partial \bar{b}}{\partial t} \quad + \quad \nabla \cdot \overline{\boldsymbol{u}}\bar{b} + \nabla \cdot \overline{\mathbf{u}'b'} = \bar{\mathcal{D}}, \qquad (4)$$

$$\frac{d\text{PE}}{dt} \quad \equiv \quad -\frac{d}{dt}\overline{zb}^{xyz} = -\overline{wb}^{xyz}. \qquad (5)$$

---

[4]Ertel potential vorticity, or PV, is $(f + \nabla \times \mathbf{u}) \cdot \nabla b$, but when averaged over the meandering front it is well-approximated by $f\bar{b}_z$.

Overlines denote averaging (Table 1).

a. Magnitude of the Potential Energy Release

A simple scaling for the magnitude of the vertical and horizontal eddy buoyancy fluxes begins by considering the PE extraction by exchange of fluid parcels over a decorrelation distance $(\Delta y, \Delta z)$ in a time Δt, as sketched in Fig. 8,

$$\frac{\Delta \text{PE}}{\Delta t} \quad \propto \quad \frac{-\Delta z \left(\Delta y M^2 + \Delta z N^2 \right)}{\Delta t}. \tag{6}$$

We may estimate the extraction rate by assuming:

1. The relevant timescale Δt is *advective*: the time it takes for an eddy to traverse the decorrelation length with typical eddy velocities, $\mathcal{V}$:

$$\Delta t \propto \Delta y / \mathcal{V}. \tag{7}$$

2. The horizontal eddy velocity, $\mathcal{V}$, scales as the mean thermal wind, U (see Fig. 5):

$$\mathcal{V} \propto U = \frac{M^2 H}{f}. \tag{8}$$

3. The vertical decorrelation length scales with the ML depth (see Fig. 6):

$$\Delta z \propto H. \tag{9}$$

4. Fluid exchange occurs along a shallower slope (*i.e.*, PE extracting) and proportional to the mean isopycnal slope (see Fig. 7):

$$\frac{\Delta z}{\Delta y} = \frac{1}{C} \frac{M^2}{N^2}, \qquad C > 1. \tag{10}$$

Thus,

$$\frac{\Delta \text{PE}}{\Delta t} \quad \propto \quad -\frac{C-1}{C} \frac{M^4 H^2}{|f|}. \tag{11}$$

Taking the absolute value of f ensures that PE is extracted in southern and northern hemispheres.

The MLE vertical flux dominates the mean, so

$$\overline{wb}^{xyz} \approx \overline{w'b'}^{xyz} \propto \frac{C-1}{C} \frac{M^4 H^2}{|f|}. \tag{12}$$

Assumption 4 implies

$$\overline{v'b'}^{xyz} = -C \frac{\overline{w'b'}^{xyz} N^2}{M^2},$$

$$\propto -\left[(C-1) \frac{N^2 H^2}{|f|} \right] M^2. \tag{13}$$

To conclude, (12) and (13) are consistent with Fig. 8: $\overline{w'b'}$ is upward and $\overline{v'b'}$ is down the mean buoyancy gradient, M^2.

b. Magnitude of the Overturning Streamfunction

One might base a parameterization of $\overline{w'b'}$ and $\overline{v'b'}$ directly on the scalings (12) and (13), but introduction of an overturning streamfunction aids numerical implementation.

The eddy buoyancy fluxes may be decomposed into a *skew* flux generated by a streamfunction $(\overline{v'_s b'} \equiv -\Psi \bar{b}_z, \overline{w'_s b'} \equiv \Psi \bar{b}_y)$ and the remaining *residual* flux,

$$\nabla \cdot \overline{\mathbf{u}'b'} \quad = \quad -\frac{\partial}{\partial y}\left(\Psi \bar{b}_z \right) + \frac{\partial}{\partial z}\left(\Psi \bar{b}_y \right) \tag{14}$$
$$+ \frac{\partial (\overline{v'b'} - \overline{v'_s b'})}{\partial y} + \frac{\partial (\overline{w'b'} - \overline{w'_s b'})}{\partial z},$$

In an adiabatic statistically-steady setting the residual flux would vanish, so all fluxes would be skew with a unique streamfunction. In spindown problems, the residual flux does not vanish–the fluxes are more horizontal than the isopycnals–primarily due to time dependence. Thus a choice of streamfunction remains, and this choice should be governed by the ease of parameterization of the residual flux (Plumb and Ferrari, 2005). Traditionally, the streamfunction is chosen to eliminate the *horizontal* residual flux (Andrews and McIntyre, 1978),

$$\Psi_{\text{tr}} \quad \equiv \quad \frac{-\overline{v'b'}}{\bar{b}_z}, \tag{15}$$

$$\nabla \cdot \overline{\mathbf{u}'b'} \quad = \quad -\frac{\partial}{\partial y}\left(\Psi_{\text{tr}} \bar{b}_z \right) + \frac{\partial}{\partial z}\left(\Psi_{\text{tr}} \bar{b}_y \right) \tag{16}$$
$$+ \frac{\partial (\overline{w'b'} + \overline{v'b'} \bar{b}_y / \bar{b}_z)}{\partial z}.$$

The residual flux here is the vertical cross-isopycnal flux. It is O(Ro) compared to the skew flux, and thus it can be neglected in the ocean interior where Ro $\ll 1$ and (15) is useful. In the ML setting, the vertical fluxes are leading order. Producing $\overline{w'b'}$ in (12) would require a delicate balance of the decomposed fluxes implied in (15) and (16) to stably produce the upgradient vertical flux *and* have it vanish at the surface: a daunting numerical task. The Held and Schneider (1999) streamfunction, Ψ_{hs}, is more convenient,

$$\Psi_{\text{hs}} \quad \equiv \quad \frac{\overline{w'b'}}{\bar{b}_y}, \tag{17}$$

$$\nabla \cdot \overline{\mathbf{u}'b'} \quad = \quad -\frac{\partial}{\partial y}\left(\Psi_{\text{hs}} \bar{b}_z \right) + \frac{\partial}{\partial z}\left(\Psi_{\text{hs}} \bar{b}_y \right) \tag{18}$$
$$+ \frac{\partial (\overline{v'b'} - \overline{v'_s b'})}{\partial y}.$$

With this definition, Ψ_{hs} is readily given by $\overline{w'b'}$ in (12) and vanishes naturally at the ocean surface. Furthermore, the horizontal residual flux is an easily parameterized downgradient flux, as $C > 1$.

Care must be taken if the scaling (12) for $\overline{w'b'}^{xyz}$ is to be used to estimate Ψ_{hs} in the definition (17). The scaling (12) applies to the large scale yz-average of $\overline{w'b'}$ while (17) requires local values in y and z of $\overline{w'b'}$ and $\bar{b}_y$. The simulations suggest that smoothing horizontally over an MLE lengthscale–or equivalently the resolution of any model where the parameterization will be used–is sufficient to quell these subtle distinctions (see FF). Thus, a local relationship in y is presumed,

$$\overline{\Psi}^z \propto \frac{(C-1)H^2\overline{b_y}^{xz}}{C|f|}. \tag{19}$$

The vertical structure of the parameterization is not local and is presented next.

c. Vertical Structure of the Overturning Streamfunction

In linear theory, the lengthscale at which the vertical velocity and the buoyancy perturbations are correlated specifies the vertical structure of $\overline{w'b'}$. Fig. 9 shows the dominant lengthscales contributing to the correlations between w', v', and b'. While the correlations and autocorrelations of v' and b' are dominated by features larger than the most unstable lengthscale, the typical horizontal scale at which w' and b' correlate remains close to L_s. The difference in correlation scales is consistent with a vertical mode saturation and an horizontal mode inverse cascade. Thus, the vertical structure of $\overline{w'b'}$ from linear theory persists at finite amplitude (per Branscome, 1983a,b).

A vertical structure function, $\mu(z)$, is taken from the $\overline{w'b'}$ of linear theory and implemented as

$$\Psi = \frac{C_e H^2 \overline{b_y}^{xz}\mu(z)}{|f|}. \tag{20}$$

Fig. 10 shows how little $\mu(z)$ changes as finite amplitude is attained. Normalization of $\mu(z)$ to peak at one collects all remaining constants into an efficiency factor C_e.

An accurate approximation of $\mu(z)$ is given by a simple extension of the analysis described in Stone (1972a). The vertical fluxes due to ageostrophic baroclinic instabilites are obtained by expanding the linear solutions to $\mathrm{O}(k^2U^2/f^2)$. The expression for $\overline{w'b'}$ is evaluated at the k of the fastest growing mode as suggested by the numerical simulations (Fig. 9).
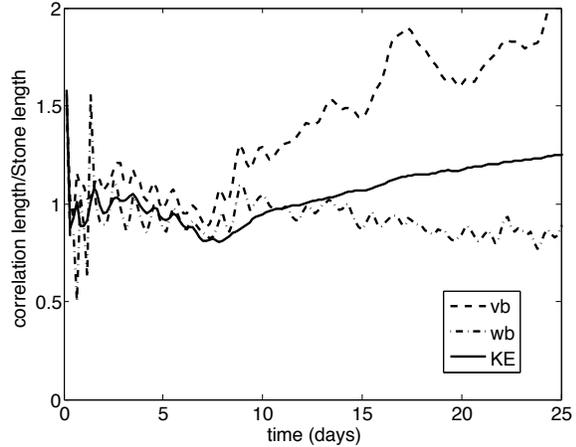
FIGURE 9: The horizontal lengthscales typical of the correlations $\overline{v'b'}$, $\overline{w'b'}$, and EKE for the same simulation as in Fig. 4 are compared to the most unstable lengthscale. Lengthscales from the v' and b' cospectrum, the w' and b' cospectrum, and the EKE spectrum, $E(k)$, are shown rescaled by the time-evolving L_s. $L^2 = \int \Re(S(k))\mathrm{d}k / \int k^2\Re(S(k))\mathrm{d}k$ for a cospectrum $S(k)$, and the $\int \Re(S(k))\mathrm{d}k$ is the full correlation. For more detail on cospectra see Emery and Thomson (2001).

Taking the large Ri limit, a $\mu(z)$ appropriate soon after MLEs begin strong restratification is found:

$$\mu(z) = \left[1 - \left(\tfrac{2z}{H}+1\right)^2\right]\left[1 + \tfrac{5}{21}\left(\tfrac{2z}{H}+1\right)^2\right]. \tag{21}$$

Below the ML base, $\mu(z)$ is set to zero. By differentiating the buoyancy budget (4) in z and averaging in the horizontal over a region large enough that the fluxes vanish on the boundaries, one finds that the dominant balance observed in the simulations:

$$\frac{\partial \overline{b_z}^{xy}}{\partial t} \approx -\overline{b_y}^x\frac{\overline{\partial^2\Psi}^y}{\partial z^2},$$

$$\approx -C_e\frac{\overline{\dfrac{H^2\left|\overline{b_y}^{xz}\right|^2}{|f|}}^y}{}\frac{\partial^2\mu(z)}{\partial z^2}. \tag{22}$$

All of the factors on the right are depth-independent except $\frac{\partial^2\mu(z)}{\partial z^2}$. Hence, $\mu(z)$ controls the relative rate of restratification at different depths.

Equations (21) and (22) suggest that restratification near the surface and base of the ML is nearly 3 times faster than in the center, consistent with numerical simulations (see FF). A long-wave approximation to $\mu(z)$ is easily obtained by neglecting the second factor in brackets in (21), as shown by Stone (1972a). This quadratic form is inappropriate for
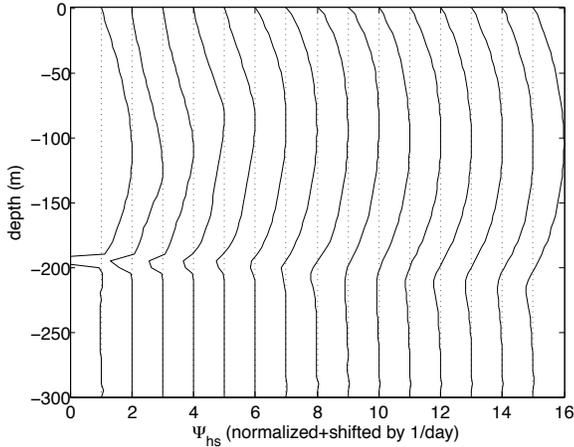
FIGURE 10: Daily snapshots of Ψ_{hs} from a typical simulation without a diurnal cycle. The streamfunctions are rescaled to have maximum of unity for comparison to $\mu(z)$ in (21), and they are shifted by 1 each day (dotted lines show the origins, ML depth $\approx$ 200m).

the ML frontal spindown, because it produces uniform restratification at all depths contrary to the result of the simulations.

d.   Comparison with other theories

Comparison with other parameterizations is useful to clarify the implications of (20). In particular, most eddy parameterizations assume a steady state with constant N^2. During ML restratification by frontal spindown both the stratification and eddy lengthscale change dramatically: this time dependence must be predicted by the parameterization rather than ignored.

Stone (1972b) uses linear instability analysis to compute the correlations $\overline{v'b'}$ and $\overline{w'b'}$ for small amplitude linear waves, and then sets the eddy velocity amplitude to be proportional to the mean flow velocity, U, as is done here. From Stone's equations 2.22-2.23,

$$\overline{v'b'} = -1.3 \left[\frac{N^2 H^2}{f} \frac{\sqrt{1+\text{Ri}}}{\text{Ri}} \right] M^2, \qquad (23)$$

$$\overline{w'b'} = 0.09 \frac{H^2 M^4}{f} \left[1 - \left(\frac{2z}{H} + 1 \right)^2 \right] \frac{1}{\sqrt{1+\text{Ri}}}. \quad (24)$$

These fluxes differ from the ones proposed here, (12) and (13), by a dependence on Ri that originates from the linear theory correlations. The difference can be traced to the linearized perturbation buoyancy budget,

$$b' \sim (M^2 v' + N^2 w')\tau_s(k), \qquad (25)$$

where τ_s is given by the linear growth timescale (3), or just $\tau_s \sim \sqrt{\text{Ri}}/f$ for large Ri. In turbulent flows, such as in Fig. 2, b' decorrelates on the much longer *advective* timescale $\tau_a \sim \text{Ri}/f$, hence the $\sqrt{\text{Ri}}$ discrepancy of Stone's formulae with the simulation results. Eddy-damped Markovian theory nicely demonstrates the transition from fluxes governed by linear timescales to fluxes governed by advective timescales as the instabilities reach finite amplitude (*e.g.,* Holloway and Kristmannsson, 1984; Salmon, 1998). A symptom of the failure of (25) is that it predicts a vertical excursion scale of $\zeta = \sqrt{\overline{b'^2}}/N^2 \propto H\tau_a/\tau_s$, while the simulations in Fig. 6 demonstrate $\zeta \propto H$.

Haine and Marshall (1998) use a mixing length argument to advocate $\overline{v'b'} \propto -L_f U M^2$, and as advocated here emphasize an advective timescale: the timescale to transfer buoyancy across the *baroclinic zone*, L_f/U. However, they presume the zone width, L_f, holds fixed during restratification. In the ML, the vertical lengthscale and vertical fluxes are more constrained than the horizontal, leading to $\Delta y \sim N^2 H/M^2$. Indeed, the snapshots in Haine and Marshall (1998) reveal eddies that enlarge beyond the initial baroclinic zone. They analyze flux scalings at only one time per simulation, τ_{model}, when 'lateral transfer by eddies has become significant', which occurs naturally when $\Delta y \sim L_f$. Their forcing provides $L_f = |N^2 H/M^2|$ initially, so

$$\overline{v'b'} \propto -L_f U M^2 \propto -\frac{N^2 H^2}{f} M^2. \qquad (26)$$

This expression agrees with (13). However, the work here uses Δy instead of L_f, which extends the evolution of $\overline{v'b'}$ and $\overline{w'b'}$ beyond τ_{model} and applies to situations where L_f is not equal to $|N^2 H/M^2|$ initially (*e.g.,* Fig. 3).

Green (1970) proposes a scaling based on equating the total difference in PE between an initial baroclinic zone and an hypothetical one with the minimum PE accessible by adiabatic rearrangement. The PE released is equated to EKE to yield an eddy velocity scale and–with b' scaling as the buoyancy difference across the zone–a scale for $\overline{v'b'}$. Green assumes constant N^2, but by adapting Green's approach to allow for large changes in N^2 yields,

$$\Delta PE \quad \propto \quad H M^2 L_f, \qquad (27)$$

$$\overline{v'b'} \quad \propto \quad -M^3 L_f^{3/2} H^{1/2} \qquad (28)$$

$$\propto \quad \frac{-M^2 N^2 H^2}{|f|} \frac{1}{\text{Ro}^{3/2} \text{Ri}^{1/2}}. \qquad (29)$$

Where Ro $= U/(fL_f)$. Once the eddy lengthscale exceeds the front width, one may replace L_f with N^2H/M^2 (or equivalently Ro with Ri^{-1}), and then (29) becomes,

$$\overline{v'b'} \propto -\frac{N^2H^2\sqrt{\text{Ri}}}{f}M^2. \qquad (30)$$

Different arguments lead Visbeck et al. (1997) and Larichev and Held (1995) to the same expression. While the amount of PE extracted in (27) is the same as proposed in Section 3a, the results for $\overline{v'b'}$ differ by $\sqrt{\text{Ri}}$. The extraction of mean PE is close to EKE+EPE, but Green assumes that EKE+EPE $\propto$ EKE. Yet, from the numerical simulations (Figs. 5 and 6),

$$\frac{\text{EKE}}{\text{EPE}} \propto \frac{M^4H^2}{f^2N^2H^2} \propto \text{Ri}^{-1}.$$

As Ri increases, the mean PE extracted goes increasingly to EPE, while EKE saturates near the initial mean KE. The work here avoids this problem by using the PE budget, (5), to directly relate PE extracted to $\overline{w'b'}^{xyz}$.

Some eddy parameterizations (*e.g.,* Canuto and Dubovikov, 2005; Eden, 2006) suppose that the decorrelation length is approximately the linear instability lengthscale for a mixing length theory. Using the linear lengthscale in (2) yields,

$$\overline{v'b'} \propto -L_sUM^2 \propto -\left[\frac{N^2H^2}{|f|}\frac{\sqrt{1+\text{Ri}}}{\text{Ri}}\right]M^2. \quad (31)$$

Except for an unspecified efficiency factor, this expression is Stone's (23). This approach fails because the linear instability lengthscale during frontal spindown is smaller than $\Delta y \propto N^2HM^{-2}$ by $L_s/\Delta y \propto \sqrt{1+\text{Ri}}/\text{Ri}$.

In summary, the scaling here differs from others in approach and by nondimensional factors. The parameterization is tested against these alternatives in Section 4.

e. Residual Diffusive Fluxes

The skew flux generates restratification because it is part of the overturning circulation, but the residual flux,

$$\mathbf{R} = \overline{v'b'} + \Psi\bar{b}_z = \overline{v'b'} + \overline{w'b'}\frac{\bar{b}_z}{\bar{b}_y}, \qquad (32)$$

merely widens the front slightly (FF). In the linear Eady model, $\overline{v'b'}$, $\bar{b}_z$, and $\bar{b}_y$ are depth-independent

while $\overline{w'b'}$ depends on $\mu(z)$, so the relationship between residual flux and $\overline{v'b'}$ is depth dependent. In these simulations $\overline{v'b'}$ and $\bar{b}_z$ change as the flow restratifies until $\mathbf{R} \approx \overline{v'b'}/2$. Perhaps not coincidentally, parcel exchange theory indicates that if $\mathbf{R}$ is $\overline{v'b'}/2$ at all depths then potential energy extraction is maximized. Using the scalings for $\overline{v'b'}$ and $\overline{w'b'}$ in (13) and (12), $\mathbf{R}$ can be parameterized with a nonlinear horizontal diffusivity scaling as

$$\overline{v'b'} + \Psi\bar{b}_z = -\kappa_H\bar{b}_y, \qquad (33)$$

$$\kappa_H = \frac{C_e\overline{b}_z^{xz}H^2\mu(z)}{|f|}. \qquad (34)$$

Given the value of $C_e \approx 0.06$ as determined in Section 4 and typical ML stratifications, κ_H is only $O(1 - 100\text{m}^2/\text{s})$. This small value confirms that MLE horizontal fluxes–residual or not–are smaller than mesoscale horizontal fluxes. FF show that in a forward simulation of parameterized frontal spindown, adding the residual flux widens the front, but minutely–comparably to changing the buoyancy advection scheme. They also show that including residual fluxes makes the model less stable numerically. In sum, adding the residual fluxes is possible, but the costs outweigh the benefit.

While $\overline{w'b'}$ is upward in the ML, it is downward below the ML base, as the reversal of the sign of Ψ just below the ML base in Fig. 10 shows. This tendency is easily understood: v' and w' are continuous, so fluxes roughly along isopycnals in the ML overshoot as the mean isopycnal slope flattens suddenly at the ML base. Below the ML base the vertical buoyancy flux is downward and thus down the mean vertical buoyancy gradient; a vertical diapycnal diffusivity κ_v of $O(10^{-4}m^2/s)$ acting on the mean buoyancy gradient could parameterize this flux. This magnitude was estimated by diagnosing $\overline{w'b'}/\bar{b}_z$ for the simulations run using the typical MLE parameter values in Table 2, but κ_v varies strongly with MLE strength. FF show that using $\kappa_v = 3\cdot10^{-5}m^2/s$ in a forward model of the parameterization slightly improves agreement with a comparable submesoscale-resolving simulation. Turbulent mixing parameterizations may already contain penetrating turbulent fluxes of this magnitude (*e.g.,* Large et al., 1994). The additional diffusivity might be important where ML entrainment is critical, but a full study of this secondary effect of MLEs is beyond the scope of the present work.
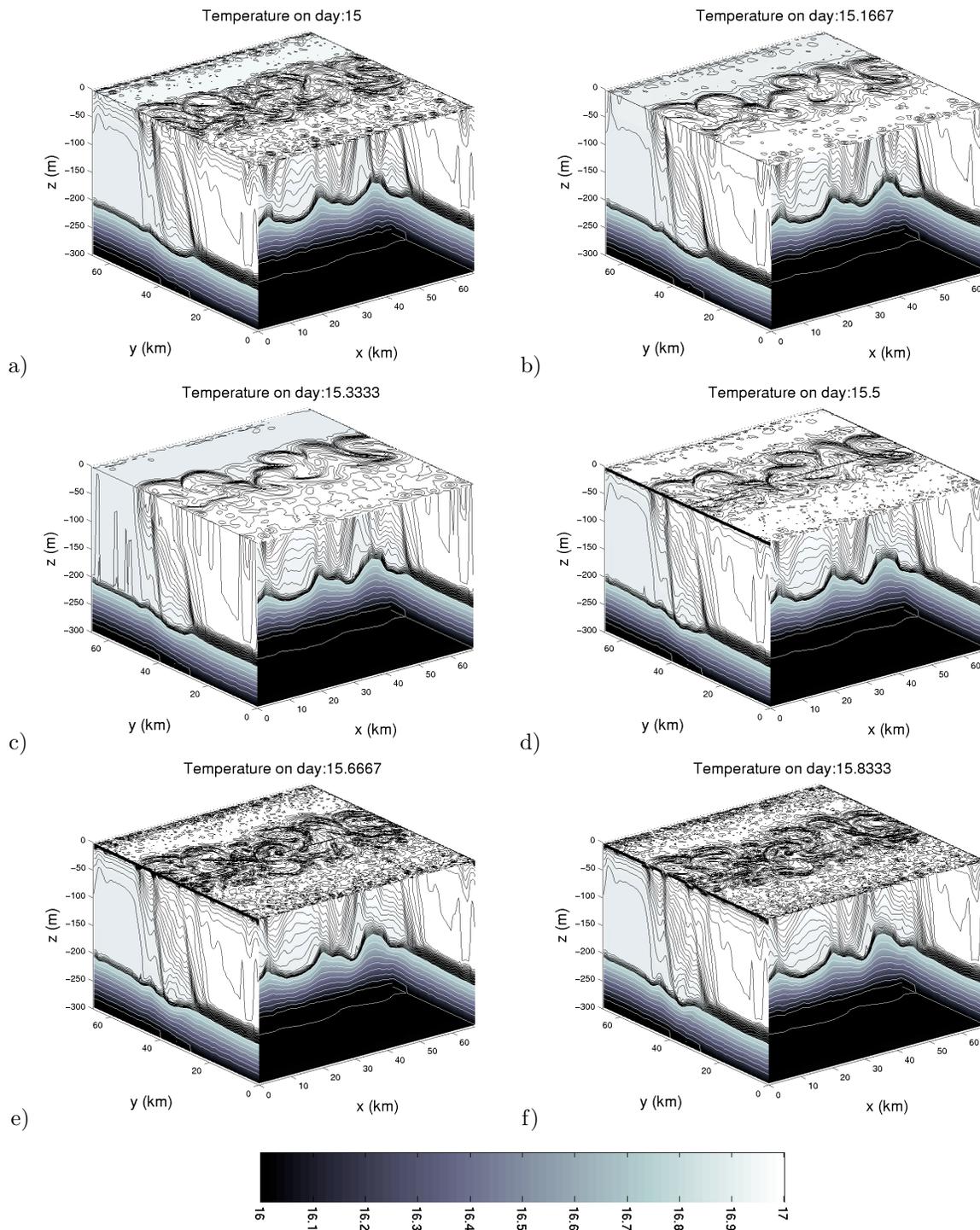
FIGURE 11: Temperature (^{o}C) during one diurnal cycle using convective adjustment. Panels d-e) are afternoon values. (Black contour interval=0.01^{o}C, white contour interval=0.1^{o}C.)

f. MLEs under Additional Mixing: Diurnal Cycle

The preceding discussion has paid little attention to the mechanisms that cause the ML to be mixed in the first place: turbulent vertical mixing. Some Rossby adjustment simulations were inundated with a diurnal heat flux cycle for a more realistic ML en-
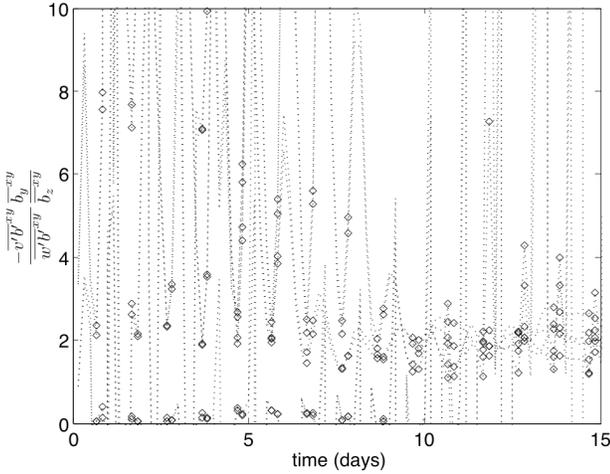
FIGURE 12: As in Fig. 7, but for a simulation with a diurnal cycle. The afternoon values, when the surface is not being actively cooled, are shown as diamonds.

FIGURE 13: Daily snapshots of afternoon Ψ_{hs} from a typical simulation with a diurnal cycle. Compare to Fig. 10.

vironment. An example is shown in Fig. 11 and Fig. 2d-f. With a diurnal cycle, the initial instability wavelength is slightly smaller during the linear growth stage (see BFF), but later the MLEs and their nonlinear saturation are remarkably similar to those in Figs. 2, 4, and 5.

Considering "afternoon" snapshots suffices to isolate the effects of MLEs; during the night convection blurs the MLE signal. Fig. 12 shows that the afternoon MLE fluxes are along a slope shallower than the isopycnal slope just as without a diurnal cycle. This effect is apparent once the MLEs are sufficiently strong to overcome the noise of the diurnal cycle (after about day 10). The next section shows that the Ψ scaling (20) holds nearly as well as in the no diurnal mixing case.

The diurnal cycle causes a notable change to the vertical structure of the fluxes. Fig. 13 shows that the streamfunction does not vanish at the surface, but at some level below. This is because the ML is capped by large N^2 during solar heating (Figs. 2 and 11). The streamfunction structure $\mu(z)$ may be trivially altered by translating and rescaling the vertical coordinate in $\mu(z)$ so that it vanishes at a depth just below the surface rather than the surface. This shortcut approximates the result from linear instability analysis for a ML with surface-intensified N^2.

In conclusion, the scaling for Ψ in (20) holds in the presence of spatially-uniform intermittent mixing due to a strong diurnal cycle, as MLEs are relatively unaffected. Haine and Marshall (1998) find

the same scaling with a constant $400\mathrm{W/m}^2$ cooling of the surface to represent strong wintertime cooling, so even larger fluxes without daytime restratification do not halt MLEs. However, MLE restratification may not overtake convective destratification. Indeed, here the basin-average ML stratification decreases each night as the MLE $\overline{w'b'}$ is dwarfed by the peak cooling. Yet, the carefully chosen balance between nighttime cooling and solar heating in these simulations is tipped by the MLE flux so that the long term tendency is toward a shallower ML. In the ocean and in realistic models a balance will exist between long-term-average (e.g., monthly) surface forcing and MLE restratification, while during active convection the effects of MLEs will be secondary. MLE restratification does not prevent active convection but immediately initiates restratification when convection ceases, during the daytime here and at the edge of the cooling region in Haine and Marshall (1998).

4. Diagnostic Validation

This section validates the scaling argument presented above by diagnosing the magnitude of the overturning streamfunction in MLE-resolving numerical simulations.

The simulations provide instantaneous 3-dimensional fields of buoyancy and buoyancy fluxes. The relevant diagnosed quantity is,

$$\Psi_{\mathrm{d}} = \frac{1}{T} \int_{t_0}^{t_0+T} \frac{\overline{w'b'}^{xy}}{\overline{b_y}^{xy}} \mu(z)^{-1} \mathrm{d}t, \qquad (35)$$

Where the time averaging in (35) is restricted to an interval after MLEs have reached finite amplitude and before lateral boundary effects are important. Appendix C discusses further details of the diagnosis.

Fig. 14a shows that Ψ_d scales well with $\overline{H^2 \overline{b_y}^{xz} |f|^{-1}}^{yt}$ for a set of 37 runs with balanced initial conditions and no diurnal cycle. The slope on this figure demonstrates the scaling, and the intercept amounts to $C_e = 0.06$ in (20). Fig. 14b shows that the same scaling holds over the whole set of 241 simulations varying front strength, initial stratification, front width, vertical and horizontal viscosity, rotation rate, *etc.* Consistent with Fig. 3, balanced and unbalanced simulations obey the same scaling. The diurnal cycle introduces noise in the estimation of Ψ_d, as can be anticipated from the noisy afternoon results in Fig. 12, and increases the estimate of C_e to near 0.08. The scaling agrees best when Ψ_d is large, which is when MLE restratification is most important (Fig. 14b).

The magnitude of C_e may be compared to other studies measuring baroclinic eddy horizontal fluxes by using the scaling for the vertical flux (12) and converting to an horizontal flux with (13). Cenedese et al. (2004) present a laboratory result for horizontal flux scaling approximately equivalent to $C_e = 0.05$, and cite many studies covering a range equivalent to $0.02 < C_e < 0.12$. The wide range found in these studies is likely an artifact of fitting inappropriate scaling laws to $\overline{v'b'}$ and consequently folding parameter variations (of Ri, for example) into the measured 'constants' of eddy processes.

A clever intuition might arrive at the scaling $\Psi \propto C_e M^2 H^2 \mu(z)/|f|$ by pure dimensional analysis, but dimensional analysis cannot rule out nondimensional parameters. Dependence on Ri is quickly eliminated. Figs. 14c-d show that the scaling of Stone (1972b) from (24) and (17),

$$\Psi_s = C_s \frac{H^2 \overline{b_y}^{xz} \mu(z)}{|f|} \frac{1}{\sqrt{1 + \text{Ri}}}, \qquad (36)$$

and Green (1970) from (30) and (15),

$$\Psi_g = C_g \frac{H^2 \overline{b_y}^{xz} \mu(z)}{|f|} \sqrt{\text{Ri}}, \qquad (37)$$

have substantially more scatter than Fig. 14a confirming the scaling proposed in (20).[5] Fig. 14f shows

---

[5]The similar scalings of Canuto and Dubovikov (2005) and Visbeck et al. (1997) are equivalent to Stone and Green and have more scatter, too.

that this scatter is associated with erroneous dependence on the time-evolving Ri, rather than other factors. (Using the initial value of Ri instead of a time-evolving value produces an order of magnitude more scatter for these scalings, not shown). Fig. 14e shows there is no systematic trend with Ri in the departures of Ψ_d from (20), nor is there a systematic trend with the initial value of Ri (not shown). Dependence on Ro through the frontal width L_f, as in (29) and as assumed by Haine and Marshall (1998) is irrelevant as soon as $\Delta y > L_f$, which occurs soon after finite amplitude is attained. A figure like Fig. 14e, but with Ro as ordinate shows no dependence on Ro (not shown).

Additional potentially relevant nondimensional quantities appear in the problem, such as (H/L_f), Smagorinsky coefficient (Sm), grid resolution to front width $(\Delta x/L_f)$, Ekman number (Ek $\equiv \nu H^{-2} f^{-1}$), diurnal cycle timescale to inertial timescale f/Ω, and interior stratification to ML stratification (N_{ml}/N_{int}). Nonlinear optimization was used to test sets of nondimensional parameters P_i to find exponents $b(i)$ and the efficiency factor C_e that reduced the difference between Ψ_d and the product of parameters, $C_e H^2 M^2 |f|^{-1} \Pi_i P_i^{b(i)}$. By this method, an Ekman number factor of approximately $\text{Ek}^{-0.2}$ was found to improve the results. No robust dependence on any other nondimensional parameter was found (*i.e.,*the exponents were less than 0.1 in magnitude). Haine and Marshall (1998) note that the parameter space needed to distinguish potential scalings is often unexplored. Even the 241 simulations here neglect some part of parameter space. Neglected regions include nonhydrostatic effects $(H/L_f = O(1))$, barotropic instabilities of the front $(\text{RiRo}^2 \ll 1)$, and viscosity sufficient to stabilize the ML instabilities. However, the scaling presented here spans the regime relevant for MLEs.

5. Summary and Conclusion

Numerical simulations and theory reveal that the ML is host to shallow frontal instabilities that act to restratify the ML. This paper presents a parameterization of the restratification by these instabilities cast as a streamfunction to represent the overturning of the front. The parameterization depends on the horizontal buoyancy gradients and provides a first attempt at incorporating the interaction of lateral gradients and vertical mixing in the ML. This parameterization will provide GCMs with a novel climate sensitivity, so far ignored by other ML parameterizations. In three dimensions, the parame-

terization takes the form,

$$\mathbf{\Psi} = C_e \frac{H^2 \nabla \overline{b}^z \times \hat{\mathbf{z}}}{|f|} \mu(z), \tag{38}$$

with C_e between 0.06 and 0.08. The vertical structure $\mu(z)$ is well approximated by

$$\mu(z) = \left[1 - \left(\frac{2z}{H}+1\right)^2\right]\left[1 + \frac{5}{21}\left(\frac{2z}{H}+1\right)^2\right]. \tag{39}$$

This parameterization produces fluxes and an eddy-induced velocity

$$\overline{\mathbf{u}'b'} \equiv \mathbf{\Psi} \times \nabla \overline{b}, \qquad \mathbf{u}^* = \nabla \times \mathbf{\Psi}. \tag{40}$$

Two companion papers (Fox-Kemper and Ferrari, 2007; Fox-Kemper et al., 2007) give further insight into the skill, implementation, and importance for climate of the parameterization.

Previous attempts to include eddy driven restratification by horizontal buoyancy gradients in ML models relied on *ad hoc* modification of the GM mesoscale eddy parameterization through tapering functions. This approach fails as the mesoscale horizontal fluxes–were they to flux along the shallow ML slopes–imply excessive vertical fluxes and restratify the ML immediately. Indeed, the GM tapering schemes are introduced precisely to avoid instantaneous ML restratification. In contrast, MLEs provide the correct amount of eddy restratification for the ML.

The approach in developing this parameterization is novel in that scaling arguments are derived directly for the overturning streamfunction instead of relying on diffusive closures for the horizontal eddy fluxes. The scaling simply constrains the streamfunction to release PE at the rate expected for baroclinic spindown. Working in terms of diffusivities offers less obvious constraints. Furthermore, the parameterization avoids parameters that are difficult in modeling practice: Ri, deformation radius, instability length scale, or the width of a 'baroclinic zone'. Only the readily available ML depth and horizontal buoyancy gradient are needed. The issue of estimating the relevant horizontal buoyancy gradient in a coarse model is discussed in Fox-Kemper et al. (2007). In principle, the approach here could be extended to a mesoscale parameterization for use in the ocean interior, but the nontrivial complications of variable background stratification are left for a future investigation.

A few observational studies prove the existence and ubiquity of MLEs. Flament et al. (1985) observe the development of small-scale eddies along a ML front that compare favorably with the phenomena here. Munk et al. (2000) have noted MLEs in photos taken by Astronaut Scully-Power. Recent observations also suggest the tendency for MLEs to release PE from fronts (D'Asaro, pers. comm.). Houghton et al. (2006) detect submesoscale along-isopycnal filaments of tracer possibly indicating frontal instabilities, although somewhat below the surface ML. Repeated MLE slumping of horizontal density fronts (formed from salinity and temperature variations) interspersed with strong vertical mixing events effectively eliminates the horizontal density fronts, but leaves behind compensated salinity and temperature gradients (Young, 1994; Ferrari and Young, 1997; Ferrari and Paparella, 2003). ML density compensation is observed at the submesoscale (Rudnick and Ferrari, 1999; Ferrari and Rudnick, 2000; Rudnick and Martin, 2002). Hosegood et al. (2006) demonstrate that density variability extends to the ML deformation radius and not beyond, in agreement with our analysis of MLEs. Rudnick and Martin (2002) show that density compensation is stronger for deep MLs. All of these observations are consistent with restratification by MLEs.

Now that a foundation has been laid, the effects of MLEs may be studied in combination with effects of wind (Thomas, 2005) and mesoscale frontogenesis (Spall, 1997; Oschlies, 2002; Lapeyre et al., 2006). Including the additional physics may improve the fundamental parameterization here. However, the results here and in FF show that for the case of nonlinear spindown of a mixed layer front this parameterization has significant skill.

A. Mesoscale-Submesoscale Resolving Model Configuration

The coupled mesoscale-submesoscale simulation is a $200km \times 600km \times 800m$ channel on an f-plane with temperatures restored near the walls to force a geostrophic flow. A sloping bottom keeps the eddies out of the temperature restoring region. The vertical resolution is 10m over the surface 100m, and then enlarges by 20% for each deeper gridpoint. The model is spun up with $\Delta x = 8$km for 900 days, interpolated and continued for 100 days at 2km resolution. Fig. 1 shows day 925.

Initially, $H = 75$m, and a 50m ML is preserved by a diurnal cycle of $200W/m^2$ nighttime cooling and just enough daytime penetrating shortwave radiation (maximum heat flux $-717W/m^2$) to give zero diurnal average. KPP (Large et al., 1994) is used to simulate ML turbulent processes. The heat flux q is:

$$q = q_0 + q_d\{\max[\cos(2\pi t), \cos(\pi t_h)] - \cos(\pi t_h)\}.$$

The constants are $q_0 = 200W/m^2$, $q_d \approx -1834W/m^2$, $t_h = 1/3day$, and t is model time in units of days. The temperatures in the upper layers are restored only on the warm side of the front.

Below H, the initial stratification is:

$$\frac{\rho}{\rho_0} = 1 - \alpha[T_0 + e^{(z+H)/\delta}(\Delta T_v + \tfrac{\Delta T_h}{2}\tanh\tfrac{y-y_0}{L})]$$
$$\Delta T_v \equiv \tfrac{T_L + T_R - 2T_0}{2}$$
$$\Delta T_h \equiv T_R - T_L$$

This stratification also is restored along the walls. Constants are ML depth (H), left temperature (T_L), right temperature (T_R), bottom temperature (T_0), thermal expansion coefficient (α), center of channel (y_0), thermocline depth scale δ and active channel width (L) and depth (D).

QG linear instability solutions are used to tune the parameters so that the most unstable modes fit in the domain. The choices used ($\Delta T_v = 5°C$, $\Delta T_h = 8°C$, $\delta = 100m$ and $D = 800m$) provide $50 - 150$km unstable modes. The fastest-growing mode is near 80km with an efolding time near 6 days. These values are smaller than those expected in the real ocean, but a sacrifice must be made for cost. Horizontal temperature gradients are rapidly mixed by the mesoscale to the boundary regions over the sloping bottom and the efolding time decreases to O(1 month). Thus, a temporal submesoscale to mesoscale scale separation is present. A robust and approximately statistically-steady mesoscale eddy field persists throughout.

B. Rossby Adjustment Model Configuration

The Rossby adjustment simulations begin with a temperature front above a stratified interior. The initial stratification is

$$\bar{b} = N^2(z + H) + \frac{L_f M_f^2}{2}\tanh\left[\frac{2(y - y_o)}{Lf}\right] + b_o,$$
$$N^2 = \begin{cases} N_{ml}^2 & \forall : z > -H_o \\ N_{int}^2 & \forall : z <= -H_o \end{cases}$$

The channel is 300m deep. The initial vertical stratification has a ML, with parameters H, M_f, N_{ml}, L_f, which rests on a more strongly stratified interior with N_{int}. Rotation rate, and viscosities are also varied (f, Sm, ν). Unbalanced or balanced initial conditions and a diurnal cycle (with $200W/m^2$ nighttime cooling as in (41)) were also used in many of the simulations. Convective adjustment was used in all simulations shown here, but test simulations in nonhydrostatic mode and with KPP (Large et al., 1994) mixing parameterization were run and gave generally similar results (see BFF). A third-order flux-limiting advection scheme was used for temperature that does not require explicit diffusion, so none was used. The selection of parameters for all 241 simulations used are given in Table 2.

C. Computation of Diagnostics

Verification of (20) begins with an along-channel mean of the fluxes and buoyancy at every time snapshot. While (20) was derived with a constant M^2 in mind, in the simulations $\bar{b}_y$ varies in cross-channel direction to isolate the front from the effects of the horizontal boundaries of the channel. Thus, care is needed in cross-channel averaging. One might average over the initial location of the center of the front, use averages weighted by $\bar{b}_y$, average only where $\bar{b}_y$ is over a critical value, or use the average over the whole channel (given that $\overline{w'b'}$ and $\bar{b}_y$ are likely to be nonzero over roughly the same region). All of these methods agree when MLEs dominate, and differ only when the signal is contaminated (e.g.,by gravity wave $\overline{w'b'}$, by the front sliding out of the averaging window, or by boundary effects). Using the basin-average is closest to (12), but averaging only over the center of the front reveals the relevant Ri. Experimentation determined that averaging over the center of the front (i.e.,where $|\bar{b}_y|$ was more than 10% of it's median value) agrees with the basin average to within 15%, so this was the y-averaging used.

Another issue is quantifying the vertical structure of the diagnosed overturning streamfunction. This is readily accomplished by evaluating the best fit to (21) (via the singular value decomposition pseudo-inverse of the discrete form of $\mu(z)$ based on a diagnosed ML depth), or more simply by taking the maximum absolute value of the streamfunction in z over the ML. Estimates agree to within a few percent, so the fit to (21) is used.

A suitable definition of H, the ML depth, is given

by the integral constraint,

$$N^2(H) = \frac{C_m}{H} \int_{-H}^{0} N^2(z')\mathrm{d}z', \qquad (41)$$

The base of the ML is the depth at which the local buoyancy frequency is C_m times the buoyancy frequency averaged from the surface. The results are relatively insensitive for $1.5 < C_m < 3$, $C_m = 2$ was used. To find H and H_s, one begins at the level of the minimum of N^2 and separates these bounds until (42) is satisfied.

$$N^2(H) = \frac{C_m}{H - H_s} \int_{-H}^{-H_s} N^2(z')\mathrm{d}z'. \qquad (42)$$

While this more complex method is used diagnostically to aid in determining the streamfunction from the MLE-resolving simulations, it is probably more complicated than needed in a parameterization where (41) will suffice.

The parameterization focuses on the period of strong restratification by finite-amplitude ML eddies. Thus, for each simulation, a time window is diagnosed. It begins when the rms v' was more than 10% of the initial maximum mean shear velocity at half of the ML gridpoints, *i.e.,* when finite amplitude is acheived. It ends if the total buoyancy difference across the channel changes by 10% for half of the ML gridpoints to avoid effects from the sidewalls. Finally, the window is restricted to times when the different y-averaging methods agree to within two standard deviations to eliminate the occasional moment when M^2 vanishes in a particular average. For runs with a diurnal cycle, the averaging window is further restricted to afternoon times. This time window generally agrees with the window one would designate 'by eye' as equilibrated, and the scaling relationships shown in all figures are supported with the 'by eye' window as well. This window simply reduces the scatter over the 'by eye' version.

The relevant diagnosed quantity is thus

$$\frac{1}{T} \int \frac{\langle \overline{w'b'} \rangle}{\langle \bar{b}_y \rangle} \mu(z)^{-1} \mathrm{d}t. \qquad (43)$$

Where $\mu(z)^{-1}$ indicates the pseudo-inverse of (21), and the time-averaging occurs only over the time window specified above.

REFERENCES

Andrews, D. G. and M. E. McIntyre: 1978, Generalized Eliassen-Palm and Charney-Drazin theorems for waves on axisymmetric flows in compressible atmospheres. *J. Atmos. Sci.*, **35**, 175–185.

Blumen, W.: 1979, On short-wave baroclinic instability. *J. Atmos. Sci.*, **36**, 1925–1933.

Boccaletti, G., R. Ferrari, and B. Fox-Kemper: 2007, Mixed layer instabilities and restratification. *J. Phys. Oceanogr.*, **35**, 1263–1278.

Branscome, L. E.: 1983a, The charney baroclinic stability problem: Approximate solutions and modal structures. *J. Atmos. Sci.*, **40**, 1393–1409.

— 1983b, A parameterization of transient eddy heat flux on a beta-plane. *J. Atmos. Sci.*, **40**, 2508–2521.

Canuto, V. M. and M. S. Dubovikov: 2005, Modeling mesoscale eddies. *Ocean Modeling*, **8**, 1–30.

Capet, X., J. McWilliams, M. J. Molemaker, and A. Shchepetkin: 2006, The transition from mesoscale to submesoscale in the california current system. *J. Phys. Oceanogr.*, submitted.

Cehelsky, P. and K. K. Tung: 1991, Nonlinear baroclinic adjustment. *J. Atmos. Sci.*, **48**, 1930–1947.

Cenedese, C., J. C. Marshall, and J. A. Whitehead: 2004, A laboratory model of thermocline depth and exchange across circumpolar fronts. *J. Phys. Oceanogr.*, **34**, 656–667.

Chanut, J., B. Barnier, W. Large, L. Debreu, T. Penduff, and J. M. Molines: 2005, Mesoscale eddies in the Labrador Sea and their contribution to convection and re-stratification. *J. Phys. Oceanogr.*, submitted.

Eady, E. T.: 1949, Long waves and cyclone waves. *Tellus*, **1**, 33–52.

Eden, C.: 2006, Towards a turbulence model for mesoscale eddies. *J. Phys. Oceanogr.*, submitted.

Emery, W. J. and R. E. Thomson: 2001, *Data Analysis Methods in Physical Oceanography*. Elsevier, Amsterdam, 2 edition, 638 pp.

Ferrari, R. and F. Paparella: 2003, Compensation and alignment of thermohaline gradients in the ocean mixed layer. *J. Phys. Oceanogr.*, **33**, 2214–2223.

Ferrari, R. and D. L. Rudnick: 2000, The thermohaline structure of the upper ocean. *J. Geophys. Res.*, **105**, 16,857–16,883.

Ferrari, R. and L. Thomas: 2007, Friction, frontogenesis, frontal instabilities and the stratification of the surface mixed layer. *J. Phys. Oceanogr.*, submitted.

Ferrari, R. and W. R. Young: 1997, On the development of thermohaline correlations as a result of nonlinear diffusive parameterizations. *J. Mar. Res.*, **55**, 1069–1101.

Flament, P., L. Armi, and L. Washburn: 1985, The evolving structure of an upwelling filament. *J. Geophys. Res.*, **90**, 11765–11778.

Fox-Kemper, B. and R. Ferrari: 2007, Parameterization of mixed layer eddies. II: Prognosis and impact. *J. Phys. Oceanogr.*, submitted.

Fox-Kemper, B., R. W. Hallberg, and R. Ferrari: 2007, Parameterization of mixed layer eddies. III: Global implementation and model impact. *J. Phys. Oceanogr.*, in preparation.

Gent, P. R. and J. C. McWilliams: 1990, Isopycnal mixing in ocean circulation models. *J. Phys. Oceanogr.*, **20**, 150–155.

Gent, P. R., J. Willebrand, T. J. McDougall, and J. C. McWilliams: 1995, Parameterizing eddy-induced tracer transports in ocean circulation models. *J. Phys. Oceanogr.*, **25**, 463–474.

Green, J. S.: 1970, Transfer properties of the large-scale eddies and the general circulation of the atmosphere. *Q. J. Roy. Meteor. Soc.*, **96**, 157–185.

Haine, T. W. N. and J. C. Marshall: 1998, Gravitational, symmetric and baroclinic instability of the ocean mixed layer. *J. Phys. Oceanogr.*, **28**, 634–658.

Hallberg, R.: 2003, The suitability of large-scale ocean models for adapting parameterizations of boundary mixing and a description of a refined bulk mixed layer model. *Proceedings of the 2003 'Aha Huliko'a Hawaiian Winter Workshop*, 187–203.

Held, I. M. and T. Schneider: 1999, The surface branch of the zonally averaged mass transport circulation in the troposphere. *J. Atmos. Sci.*, **56**, 1688–1697.

Holloway, G. and S. S. Kristmannsson: 1984, Stirring and transport of tracer fields by geostrophic turbulence. *J. Fluid Mech.*, **141**, 27–50.

Hosegood, P., M. Gregg, and M. Alford: 2006, Sub-mesoscale lateral density structure in the oceanic surface mixed layer. *Geophys. Res. Lett.*, submitted.

Hoskins, B. J.: 1976, Baroclinic waves and frontogenesis. Part I: Introduction and eady waves. *Quart. J. Roy. Meteor. Soc.*, **102**, 103–122.

Houghton, R. W., D. Hebert, and M. Prater: 2006, Circulation and mixing at the New England shelfbreak front: Results of purposeful tracer experiments. *Progress in Oceanography*, **70**, 289–312.

Howells, I. D.: 1960, An approximate equation for the spectrum of a conserved scalar quantity in a turbulent fluid. *J. Fluid Mech.*, **9**, 104–106.

Jones, H. and J. Marshall: 1993, Convection with rotation in a neutral ocean: A stude of open-ocean deep convection. *J. Phys. Oceanogr.*, **23**, 1009–1039.

— 1997, Restratification after deep convection. *J. Phys. Oceanogr.*, **27**, 2276–2287.

Killworth, P. H.: 2005, On the parameterisation of eddy effects on mixed layers and tracer transports: a linearised eddy perspective. *J. Phys. Oceanogr.*, **35**, 1717–1725.

Kraus, E. B. and J. S. Turner: 1967, A one-dimensional model of the seasonal thermocline. *Tellus*, 88–97.

Lapeyre, G., P. Klein, and B. L. Hua: 2006, Oceanic restratification forced by surface frontogenesis. *J. Phys. Oceanogr.*, **36**, 1577–1590.

Large, W. G., J. C. McWilliams, and S. C. Doney: 1994, Oceanic vertical mixing: A review and a model with a vertical k-profile boundary layer parameterization. *Rev. Geophys.*, 363–403.

Larichev, V. D. and I. M. Held: 1995, Eddy amplitudes and fluxes in a homogeneous model of fully developed baroclinic instability. *J. Phys. Oceanogr.*, **25**, 2285–2297.

Mahadevan, A.: 2006, Modeling vertical motion at ocean fronts: Are nonhydrostatic effects relevant at submesoscales? *Ocean Modelling*, **14**, 222–240.

Mahadevan, A. and A. Tandon: 2006, An analysis of mechanisms for submesoscale vertical motion at ocean fronts. *Ocean Modelling*, **14**, 241–256.

Marshall, J. C., A. Adcroft, C. Hill, L. Perelman, and C. Heisey: 1997, A finite-volume, incompressible Navier-Stokes model for studies of the ocean on parallel computers. *J. Geophys. Res.*, **102**, 5753–5766.

Molemaker, M. J., J. C. McWilliams, and I. Yavneh: 2005, Baroclinic instability and loss of balance. *J. Phys. Oceanogr.*, **35**, 1505–1517.

Munk, W., L. Armi, K. Fischer, and Z. Zachariasen: 2000, Spirals on the sea. *Proc. Roy. Soc. Lond. A*, **456**, 1217–1280.

Nakamura, N.: 1988, Scale selection of baroclinic instability–Effects of stratification and nongeostrophy. *J. Atmos. Sci.*, **45**, 3253–3268.

— 1994, Nonlinear equilibration of two-dimensional eady waves: Simulations with viscous geostrophic momentum equations. *J. Atmos. Sci.*, **51**, 1023–1035.

Nakamura, N. and I. M. Held: 1989, Nonlinear equilibration of two-dimensional eady waves. *J. Atmos. Sci.*, **46**, 3055–3064.

Nurser, A. J. G. and J. W. Zhang: 2000, Eddy-induced mixed layer shallowing and mixed layer/thermocline exchange. *J. Geophys. Res.*, **105**, 21,851–21,868.

Oschlies, A.: 2002, Improved representation of upper-ocean dynamics and mixed layer depths in a model of the north atlantic on switching from eddy-permitting to eddy-resolving grid resolution. *J. Phys. Oceanogr.*, **32**, 2277–2298.

Ou, H. W.: 1984, Geostrophic adjustment: A mechanism for frontogenesis? *J. Phys. Oceanogr.*, **14**, 994–1000.

Plumb, R. A. and R. Ferrari: 2005, Transformed Eulerian mean theory. Part I: Nonquasigeostrophic theory for eddies on a zonal-mean flow. *J. Phys. Oceanogr.*, **35**, 165–174.

Price, J. F.: 1981, Upper ocean response to a hurricane. *J. Phys. Oceanogr.*, **11**, 153–175.

Price, J. F., R. A. Weller, and R. Pinkel: 1986, Diurnal cycling: Observations and models of the upper ocean response to diurnal heating, cooling, and wind mixing. *J. Geophys. Res.*, **91**, 8411–8427.

Rossby, C. G.: 1937, On the mutual adjustment of pressure and velocity distributions in certain simple current systems. i. *J. Mar. Res.*, **1**, 15–28.

— 1938, On the mutual adjustment of pressure and velocity distributions in certain simple current systems. ii. *J. Mar. Res.*, **2**, 239–263.

Rudnick, D. L. and R. Ferrari: 1999, Compensation of horizontal temperature and salinity gradients in the ocean mixed layer. *Science*, **283**, 526–529.

Rudnick, D. L. and J. P. Martin: 2002, On the horizontal density ratio in the upper ocean. *Dyn. Atmos. Oceans*, **36**, 3–21.

Salmon, R.: 1998, *Lectures on Geophysical Fluid Dynamics*. Oxford University Press, New York, 378 pp.

Samelson, R. M. and D. C. Chapman: 1995, Evolution of the instability of a mixed-layer front. *J. Geophys. Res.*, **100**, 6743–6759.

Schneider, T. and C. C. Walker: 2006, Self-organization of atmospheric macroturbulence into critical states of weak nonlinear eddy-eddy interactions. *J. Atmos. Sci.*, **63**, 1569–1586.

Spall, M.: 1997, Baroclinic jets in confluent flow. *J. Phys. Oceanogr.*, **27**, 381–402.

— 2000, Generation of strong mesoscale eddies by weak ocean gyres. *J. Mar. Res.*, **58**, 97–116.

Stone, P. H.: 1966, On non-geostrophic baroclinic stability. *J. Atmos. Sci.*, **23**, 390–400.

— 1970, On non-geostrophic baroclinic stability: Part II. *J. Atmos. Sci.*, **27**, 721–726.

— 1972a, On non-geostrophic baroclinic stability: Part III. The momentum and heat transports. *J. Atmos. Sci.*, **29**, 419–426.

— 1972b, A simplified radiative-dynamical model for the static stability of rotating atmospheres. *J. Atmos. Sci.*, **29**, 405–418.

Tandon, A. and C. Garrett: 1994, Mixed layer restratification due to a horizontal density gradient. *J. Phys. Oceanogr.*, **24**, 1419–1424.

— 1995, Geostrophic adjustment and restratification of a mixed layer with horizontal gradients above a stratified layer. *J. Phys. Oceanogr.*, **25**, 2229–2241.

Thomas, L. N.: 2005, Destruction of potential vorticity by winds. *J. Phys. Oceanogr.*, **35**, 2457–2466.

Visbeck, M., J. C. Marshall, T. Haine, and M. Spall: 1997, Specification of eddy transfer coefficients in coarse resolution ocean circulation models. *J. Phys. Oceanogr.*, **27**, 381–402.

Weller, R. A.: 1991, Overview of the Frontal Air-Sea Interaction Experiment (FASINEX): A study of air-sea interaction in a region of strong oceanic gradients. *J. Geophys. Res.*, **96**, 8501–8516.

Young, W. R.: 1994, The subinertial mixed layer approximation. *J. Phys. Oceanogr.*, **24**, 1812–1826.
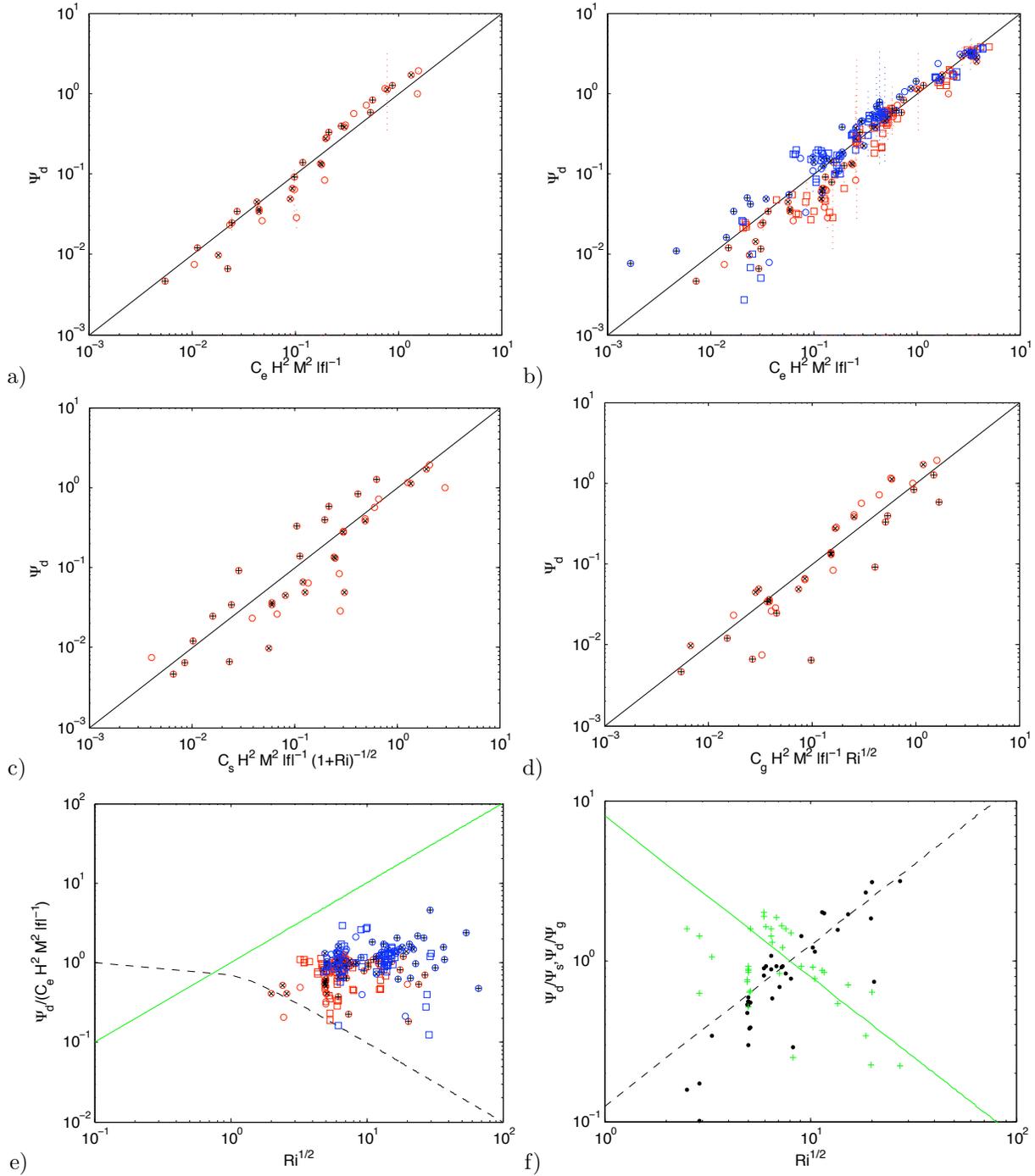
FIGURE 14: Magnitude of Ψ_d versus theories for magnitude of Ψ for simulations with diurnal cycle (blue) and without (red) starting from balanced (circles) or unbalanced (squares) initial conditions. Plus signs and crosses indicate balanced simulations where $\mathrm{Ri}_0 > 1$ or $\mathrm{Ri}_0 < 1$ initially. a) Shows Ψ_d in the balanced, no diurnal cycle simulations versus $\overline{\overline{C_e \overline{b_y}^{xz}} H^2 |f|^{-1}}^{yt}$, $C_e = 0.06$, and b) includes unbalanced and diurnal cycle simulations, $C_e = 0.08$. c) Shows Stone's theory, (36), $C_s = 0.53$. d) Shows Green's theory, (37), $C_g = 0.0085$. e) $\Psi_d / \overline{\overline{C_e \overline{b_y}^{xz}} H^2 |f|^{-1}}^{yt}$ versus $\mathrm{Ri}^{1/2}$. Also shown are lines parallel to $\mathrm{Ri}^{1/2}$ and $(1 + \mathrm{Ri})^{-1/2}$. f) Ψ_d / Ψ_s (black dots) and Ψ_d / Ψ_g (green crosses) versus $\mathrm{Ri}^{1/2}$. Also shown are lines parallel to $\mathrm{Ri}^{\pm 1/2}$. Ψ_d, Ψ_s, and Ψ_g are defined in (35), (36), and (37).

Symbol	Name	Typical Value
H	ML depth	100m
b	buoyancy ($b = -g\rho/\rho_0$, $\rho_0 = 1035\mathrm{kg/m}^3$, $g = 9.81\mathrm{m/s}^2$)	$\pm 0.04\mathrm{m/s}^2$
u, v, w	velocity components	$\pm 0.05\mathrm{m/s}$
$\mathbf{u}_H$	horizontal velocity	$\pm 0.05\mathrm{m/s}$
$\overline{A}$	along-channel mean of A and perturbation from $\overline{A}$	
$\overline{A}^{xy}$	along and cross-channel mean	
$\overline{A}^{xyz}$	horiz. mean and vert. mean over ML	
$\mathcal{V}, \mathcal{W}$	typical eddy velocity scales	$0.05 m/s$
U	mean shear velocity scale ($M^2 H/f$)	$0.05 m/s$
M^2	front-averaged horiz. buoy. gradient	$-(2f)^2$
N^2	front-averaged vert. buoy. gradient (buoy. freq.^{2})	
M_f^2	initial maximum horiz. buoy. gradient	$-(2f)^2$
N_{ml}^2, N_{int}^2	initial ML and interior vert. buoy gradient	$(4f, 64f)^2$
Ω	earth angular frequency ($2\pi/\mathrm{day}$)	$7.29 \times 10^{-5}\mathrm{s}^{-1}$
f	Coriolis parameter	Ω
τ_s	Stone growth timescale	1 day from (3)
L_s, k_s	Stone fastest-growing lengthscale/wavenumber	1km from (2)
$E(\kappa)$	kinetic energy power density spectrum ($\overline{|\overline{\mathbf{u}_H' b'}|^2}^{xyz} = \int E(\kappa)\mathrm{d}\kappa$)	
$E_s(\kappa)$	kinetic energy power density spectrum prediction from (1)	
KE, EKE	kinetic energy, eddy kinetic energy	
PE, EPE	potential energy, eddy potential energy	
Ψ_{tr}	traditional streamfunction $-\overline{v'b'}/N^2$	
Ψ_{hs}	Held & Schneider streamfunction $\overline{w'b'}/M^2$	
Ψ_{d}	diagnosed streamfunction	
$\boldsymbol{\Psi}$	3d streamfunction	
$\mathbf{u}^*$	3d eddy-induced velocity	
$\Delta x, \Delta z$	horizontal and vertical grid spacing	$L_s/10$ from (2)
L_f, L_b	front width, basin width	$40\Delta x, 150\Delta x$
x, y, z	along-channel, cross-channel, and vert. coordinate	$0 \to L_b, -300 \to 0m$
C	flux slope to isopycnal slope ratio, $-M^2\overline{v'b'}/(\overline{w'b'}N^2)$	2
C_e	efficiency factor	$0.06 - 0.08$
C_s	efficiency factor (Stone parameterization)	$0.1 - 0.9$
C_g	efficiency factor (Green parameterization)	$0.001 - 0.009$
k, l	along- and cross-channel wavenumbers	$1/L_b \to 1/\Delta x$
κ	isotropic wavenumber ($\sqrt{k^2 + l^2}$)	$1/L_b \to 1/\Delta x$
ζ	vertical excursion scale $\sqrt{\overline{b'^2}}/N^2$	$0.2H$
Ri_0	initial cond. balanced Richardson number $\mathrm{Ri}_0 = N_0^2 f^2/M_0^4$	$0 \to 256$
Ri	balanced Richardson number $\mathrm{Ri} = N^2 f^2/M^4$	$0 \to 4500$
Sm	Smagorinsky coefficient (horiz. visc.$= \left[\frac{\mathrm{Sm}\Delta x}{\pi}\right]^2 \sqrt{(u_x - v_y)^2 + (u_y + v_x)^2}$)	1
ν	vertical viscosity	$0.0001\mathrm{m}^2/\mathrm{s}$
κ_v, κ_H	vert. and horiz. MLE effective diffusivity	

TABLE 1: Symbols used in this paper.

Symbol	Name	Value Range
H	ML depth	$\{50, 200\}$m
M_f^2	horiz. buoy. gradient	$-(\{1, 2, 4\}f)^2$
N_{ml}	|ML vert. buoy. gradient|$^{1/2}$ (Buoy Freq.)	$\{0, 4, 16, 32\}f$
N_{int}	|interior vert. buoy. gradient|$^{1/2}$ (Buoy Freq.)	$\{16, 64, 128\}f$
f	Coriolis parameter	$\{2\Omega, \Omega, \Omega/2\}$
Δx	standard horiz. grid	$L_s/10$ from (2)
Δx	tripled resolution test grid	$L_s/30$ from (2)
Δz	standard vert. grid	5m
Δz	vertical test grid	1m
q_0	nightime cooling	$\{0, 200\}$W/m^2
L_f	front width	$\{20, 40, 80\}\Delta x$
Sm	Smagorinsky coefficient	$\{1, 2, 4, 8\}$
ν	vertical viscosity	$\{0.0001, 0.001, 0.01\}$m^2/s

TABLE 2: Parameters varied across simulations. Test grids were confirmed to agree with standard grids.